

MaNGA AGN dwarf galaxies (MAD) - III. The role of mergers and environment in AGN activity in dwarf galaxies

A. Eróstegui^{1,*}, M. Mezcua^{1,2}, M. Siudek^{1,3}, H. Domínguez Sánchez⁴, V. Rodríguez Morales¹

¹ Institute of Space Sciences (ICE, CSIC), Campus UAB, Carrer de Magrans, s/n, 08193 Barcelona, Spain

² Institut d'Estudis Espacials de Catalunya (IEEC), Edifici RDIT, Campus UPC, 08860 Castelldefels (Barcelona), Spain

³ Instituto de Astrofísica de Canarias, Av. Vía Láctea, s/n, E38205 La Laguna, Spain

⁴ Instituto de Física de Cantabria (IFCA, CSIC), Avda. de los Castros, s/n, 39005 Santander, Spain

Received MM DD, YY; accepted MM DD, YY

ABSTRACT

Context. Investigating whether and how galaxy mergers affect black hole growth can be determinant for black hole-galaxy evolution models and, in particular, for understanding how early Universe seed black holes grew to become supermassive. However, while mergers have been observed to enhance the active galactic nucleus (AGN) activity, and thus black hole growth in massive galaxies, it is yet not known how this relation and the role of the environment translates to dwarf galaxies (the most likely hosts of the early seed black holes), since there are scarce and mixed results in the literature.

Aims. We want to assess the impact of galaxy mergers and the environment on AGN triggering in dwarf galaxies.

Methods. We use a sample of 3280 dwarf galaxies with integral-field spectroscopic data from the MaNGA survey to study the AGN fraction throughout the merger process and how it is affected by the environment (characterized by galaxy isolation, being in a void, and group richness). We also compare the fraction of interacting galaxies in AGN and non-AGN dwarf galaxies.

Results. We find that dwarf galaxy mergers can ignite AGNs at separations below 20 kpc. The AGN fraction increases notoriously after the first pass and remains enhanced until the final stage. Despite this, mergers are not the dominant AGN triggering mechanism. We also find that the environment has a non-negligible impact on AGN activity in dwarf galaxies, as the AGN fraction increases when moving to lower density environments. These findings provide the most statistically robust constraints to date on the effects of dwarf galaxy mergers and environment on AGN activity and black hole growth.

Key words. Galaxies: dwarf – Galaxies: interactions – Galaxies: active – (*Galaxies:*) intergalactic medium

1. Introduction

A detailed model of the growth history of supermassive black holes (SMBH; $\geq 10^6 M_{\odot}$) can be determinant to unveil their origin. The detection of SMBHs at redshifts beyond $z = 10$ (Maiolino et al. 2024) suggests they had to start out as seed intermediate-mass black holes (IMBHs; $10^2 < M_{\text{BH}} \lesssim 10^6 M_{\odot}$) at even higher redshifts. Massive black holes (i.e. SMBHs and IMBHs) grow mainly via accretion (Volonteri 2010), observed as an active galactic nucleus (AGN), and coalescence with other massive black holes (e.g. Goulding et al. 2019), which could be detected via gravitational waves or, at times earlier than the coalescence, as a binary or dual AGN. Although BH coalescence is evidently consequential to a galaxy merger, it is also believed that AGN activity is ignited or enhanced during a galactic merger, as this process provides the gas necessary to build the central stellar mass and feed the SMBH (Hopkins et al. 2006; Wild et al. 2007). In fact, in the massive galaxy regime the presence of AGNs has been observed to be related to interacting galaxies (e.g. Ellison et al. 2011, 2013; Satyapal et al. 2014; Blecha et al. 2018; Steffen et al. 2023; Barrows et al. 2023; Li et al. 2023). However, very few works have studied this relation focusing in the dwarf galaxy regime (stellar mass

$M_{\star} \leq 10^{10} M_{\odot}$)¹, producing mixed results so far (Kaviraj et al. 2019; Bichang'a et al. 2024; Mičić et al. 2024). Having knowledge on how galaxy mergers affect AGN activity at different mass scales is of special importance in order to construct a precise model of BH growth history, and more so for dwarf galaxies since they are the dominant population at all redshifts (e.g. Martin et al. 2019; Driver et al. 2022) and, according to the hierarchical model of galaxy formation, give origin to massive galaxies and their respective SMBHs. Moreover, local dwarf galaxies are thought to have a quieter merger history than primordial galaxies in the same mass range, and consequently the mass of their IMBHs is expected to not have grown significantly through BH coalescence and accretion, so they could still hold some dependence on the initial seed BH mass (Van Wassenhove et al. 2010). However, dwarf galaxies undergo on average three major mergers after their formation (Fakhouri et al. 2010), each of which could lead to the coalescence of the central BHs and trigger rapid BH accretion, resulting in the BH growing significantly (Deason et al. 2014). In this case, the IMBHs in local dwarf galaxies should not be treated as relics of the early Universe seed BHs (Mezcua 2019). It is not yet clear if BH coalescence and rapid BH accretion occur in dwarf galaxies. In the case of the former, the dynamical friction of dwarf galaxies might not be efficient enough to remove the necessary angular momentum to form a

¹ Although there is not a consensus on the mass upper limit of dwarf galaxies, this value has been adopted by several authors (e.g. Paudel et al. 2018; Manzano-King & Canalizo 2020; Bichang'a et al. 2024).

* e-mail: erostegui@ice.csic.es

close BH binary, and consequently the BHs might not merge (Tamfal et al. 2018). As for the latter, no binary nor dual AGN systems have yet been confirmed in dwarf galaxies and the effect (or lack thereof) of dwarf galaxy mergers on AGN triggering remains unestablished. This very last point is the main problem we address in this work.

Another important aspect to take into account is the impact of the environment on AGN activity. The presence of AGNs in different environments has been studied by several authors, finding higher AGN fractions for massive galaxies in the field and lower density regions (e.g. Kauffmann et al. 2004; Silverman et al. 2009; Sabater et al. 2013; Ehlert et al. 2013; Lopes et al. 2017), although others found no to very weak environmental dependence (e.g. Martini et al. 2007; Pimbblet et al. 2012; Man et al. 2019), and even for the dwarf galaxy regime (Amiri et al. 2019; Siudek et al. 2022). Settling what environmental conditions (if any) affect AGN triggering in dwarf galaxies is also necessary to constrain the BH growth history model. In this work we investigate how the AGN fraction of dwarf galaxies evolves throughout different stages of the galaxy merger process with unprecedented statistical robustness, and how it is affected by three environmental factors: isolation, voids and group richness. We also investigate the extent to which galaxy mergers can account for the AGN population in dwarf galaxies. The sample, its classification and processing are described in Sect. 2, the results are reported in Sect. 3 and conclusions presented in Sect. 4. Throughout the paper we assume a Λ -CDM cosmology with parameters $H_0 = 73 \text{ km s}^{-1} \text{ Mpc}^{-1}$, $\Omega_\Lambda = 0.73$ and $\Omega_b = 0.27$.

2. Data and classification

MaNGA (Mapping Nearby Galaxies at Apache Point Observatory) is an integral-field spectroscopy survey carried out with the SDSS 2.5 m telescope (Gunn et al. 2006) as part of SDSS-IV (Blanton et al. 2017). The final data release (DR17; Abdurro'uf et al. 2022) contains all the observations and science data products for the complete survey, which includes over 10,000 galaxies with redshifts up to $z = 0.15$ that have been selected from the NASA-Sloan Atlas (NSA²; Wake et al. 2017). MaNGA makes use of 17 integral-field units (IFU) that vary in diameter from 12'' to 32'' (19 to 127 fibers with 2'' of diameter) and has a wavelength coverage of 3600-10300 Å with a spectral resolution of $R \sim 2000$ and instrumental velocity dispersion of 70 km s^{-1} (1σ ; Law et al. 2021; Yan et al. 2015). The parent sample used in this paper is detailed in Mezcua & Domínguez Sánchez (2024), and it consists of 3306 galaxies drawn from MaNGA DR17 by considering only those galaxies with Petrosian and Sérsic NSA stellar masses consistent within 0.5 dex (Secrest & Satyapal 2020), then selecting galaxies with stellar mass $M_\star \leq 10^{10} M_\odot$, and finally removing duplicates according to the DUPL_GR parameter from the *MaNGA Deep Learning Morphology catalog* (Domínguez Sánchez et al. 2021). For this work we removed from the sample those galaxies with $z > 0.06$ (4) and $z < 0.005$ (11), as they are too few and sparsely sampled, so they cannot be properly matched in the control sample. We also removed another 11 galaxies due to different issues found during the inspection (e.g. wrong NSA redshifts, not being a galaxy, MaNGA field centered on a different object). The final sample is composed of 3280 MaNGA dwarf galaxies. Figure 1 shows the stellar mass and redshift distribution of the main sample.

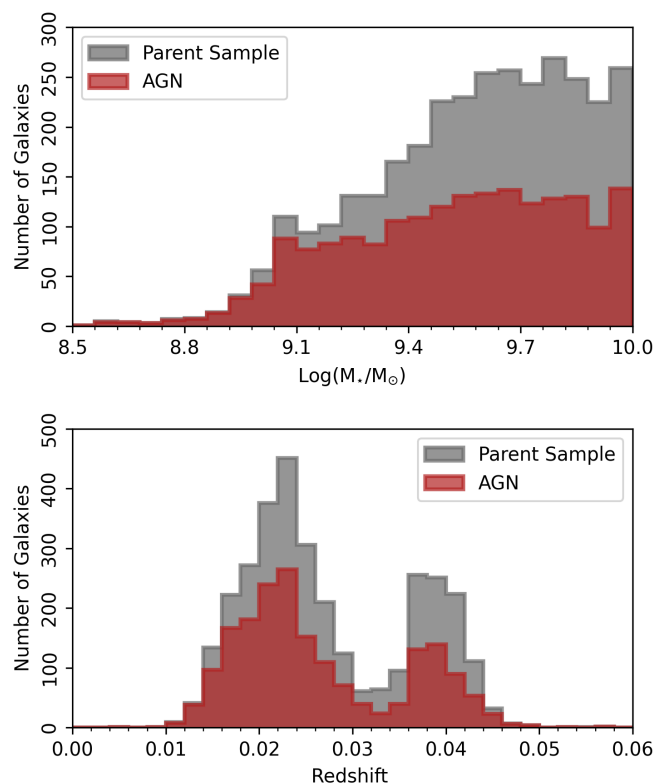


Fig. 1. Distribution of the NSA Petrosian stellar masses (top) and redshift (bottom) of the final sample of 3280 unique dwarf galaxies and the subset of galaxies that are classified as AGN (see Sect. 2.1).

2.1. AGN selection

Here we give a brief summary of the AGN classification of our sample, which is detailed in Mezcua & Domínguez Sánchez (2024). To identify AGNs the IFU spaxels were classified based on the [NII]-BPT, [SII]-BPT and [OI]-BPT optical emission line diagnostic diagrams with the Kewley et al. (2001, 2006) and Kauffmann et al. (2003) demarcation lines to differentiate between AGN, star-formation (SF), and Composite (mixture of AGN and SF) ionization in the [NII]-BPT, and between Seyfert, SF, and LINER³ ionization in the [SII]-BPT and [OI]-BPT. Additionally, the WHAN diagram (Cid Fernandes et al. 2010) was used to differentiate between true AGN ($H\alpha$ equivalent width (EW) $\geq 3 \text{ \AA}$ and flux ratio $\log [\text{NII}]/H\alpha \geq -0.4$) and SF. Based on the combination of the outcomes of all diagrams, spaxels were then classified as AGN, AGN-WHAN, Composite, SF-AGN⁴, LINER or SF. Then, spaxels with a signal-to-noise ratio $S/N \geq 3$ and unmasked stellar velocity and stellar velocity dispersion were considered as valid, and based on if the ratio of class to valid spaxels was 5% or higher the galaxies were classified as AGN, AGN-WHAN, SF-AGN, Composite or LINER. Lastly, only sources with more than 20 AGN spaxels in total were selected, which resulted in 2292 galaxies with strong indication of AGN ionizations, of which 634 are robust AGN (AGN+WHAN), 1164 SF-AGN, 114 Composite, and 165 LINERs. Figure 2 shows an example of the spatially-resolved spaxel

³ Low ionization nuclear emission line region.

⁴ These are spaxels that were classified as SF in the [NII]-BPT but as Seyfert in the [SII]- or [OI]-BPT, unlike composite spaxels which are classified as such in the [NII]-BPT, and as SF or LINER in the [SII]- or [OI]-BPT.

² <http://www.nsatlas.org>

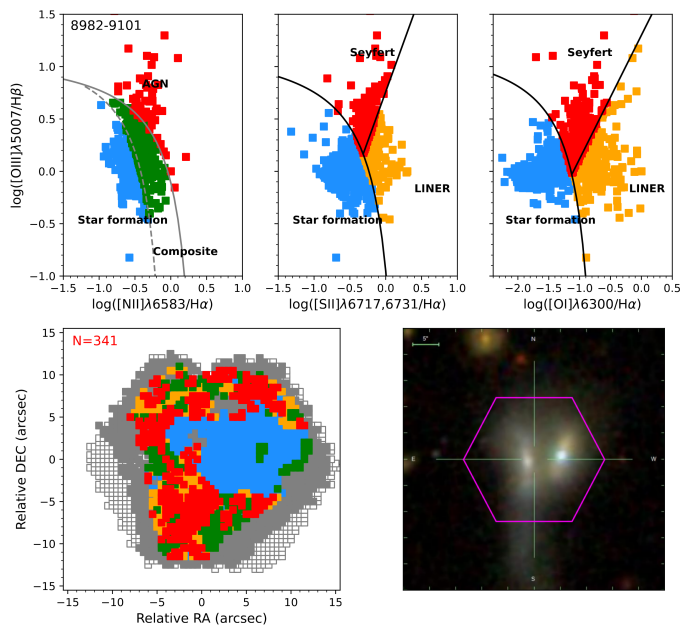


Fig. 2. MaNGA analysis of the AGN dwarf galaxy 8982-9101. Top row: Location of each MaNGA spaxel on the [NII]-BPT (left), [SII]-BPT (middle), and [OI]-BPT (right) used to distinguish between ionization by AGN (red spaxels), star-formation (blue spaxels), Composite (green spaxels), and LINER (orange spaxels). Bottom left: Spatial distribution of the BPT-classified spaxels (color-coded as in the upper panels). Empty squares mark the IFU coverage, gray squares those spaxels with continuum signal-to-noise ratio $S/N \geq 1$. The red “N” indicates the number of AGN spaxels. Bottom right: SDSS composite image. The pink hexagon shows the MaNGA field of view.

by spaxel emission line diagnostic classification. For the purposes of this work, we have reduced the classification into only two categories: AGN, which includes robust AGN, SF-AGN and Composite, adding to a total of 1899 galaxies; and non-AGN, composed of the rest of the sample, which add to a total of 1381.⁵ We have considered LINERS as non-AGN since their observed emission has been shown to be not necessarily related to AGN (e.g. Singh et al. 2013; Belfiore et al. 2016). Moreover, we found that our results remain qualitative the same if we count LINERS as AGN, although with slightly higher AGN fractions in general. With this considered, we measure the AGN fraction as:

$$f_{\text{AGN}} = \frac{N_{\text{AGN}}}{N_{\text{AGN}} + N_{\text{non-AGN}}}, \quad (1)$$

where N_{AGN} and $N_{\text{non-AGN}}$ are the number of AGN and non-AGN galaxies, respectively.

2.2. Merger classification

In order to study different properties of galaxies throughout the merging process, several authors (e.g. Larson et al. 2016; Smith et al. 2018; Pan et al. 2019) have defined a set of merger stages analogous to the Toomre sequence (Toomre 1977), based mainly on visual and morphological features. In a similar effort, we have defined a merger stage sequence as follows:

- Stage 0 (single galaxy): A single, non-interacting and non-paired galaxy.

⁵ Both numbers are obtained after applying the $z \geq 0.005$ and $z \leq 0.06$ cuts and removing the 11 erroneous galaxies.



Fig. 3. DESI Legacy composite images of galaxies representing the merger sequence defined in this work.

- Stage 1 (close pair): Separated galaxies with no signs of interaction and with projected separation $r_p \leq 50$ kpc and velocity separation $|\Delta v| \leq 300$ km s⁻¹.
- Stage 2 (early merger): Presumably post-first pass. Distinct galaxies with strong bridges, tails and/or other tidal features.
- Stage 3 (merger): Common envelope, two distinguishable nuclei and strong tidal features.
- Stage 4 (late merger): Single nucleus, highly-disturbed morphology and strong tidal features.
- Stage 5 (remnant): Single nucleus, less disturbed central morphology, tidal features (especially shells) and possibly off-center nucleus.

Figure 3 shows examples for each stage sequentially and several additional examples are displayed in Fig. B.1. We have classified our sample in accordance to this sequence in two complementary steps: visual inspection and pair selection.

2.2.1. Visual inspection

In this step we visually classify the parent sample of 3280 dwarf galaxies according to the criteria shown above, using the best image available in terms of depth and resolution. This includes images from the DESI Legacy Imaging Surveys (Dey et al. 2019), the Hyper Suprime-Cam Subaru Strategic Program DR2 (HSC; Aihara et al. 2019), the Hyper Suprime-Cam Legacy Archive (HSCLA; Tanaka et al. 2021), SDSS (York et al. 2000) and the *Hubble Space Telescope* (HST), as available in the *ALADIN interactive sky atlas* (Bonnarel et al. 2000). With some exceptions, galaxies in stage 1 were not classified as such with the visual inspection, but rather by the pair selection procedure (see Sect. 2.2.2 below). Stages 2 through 5 were classified via visual inspection. An issue to consider with this method is that the distinction between stages 1-2 and 4-5 may be held to certain ambiguity, mainly due to two reasons: the degree of disturbance and strength of the tidal features used to divide these stages depend on the criteria of the inspector, which can produce a less objective classification, and the deepest imaging survey available is not the same for all galaxies, meaning that some tidal features may be present but not detected for galaxies observed in less sensitive imaging surveys, as illustrated in Fig. 4. To account for both issues we made a finer classification procedure which is detailed in Sect. B



Fig. 4. The MaNGA galaxy 11836-3701 in composite color images from SDSS (left), DESI-Legacy (middle) and HSC (right). The bands composing the images are *gri* for SDSS and HSC, and *grz* for DESI-Legacy. Tidal features that were not visible in SDSS become noticeable in DESI-Legacy and further in HSC.

2.2.2. Galaxy pair selection

Given that the redshift distribution of our sample lies mainly between 0.01 and 0.06, deviations from the Hubble flow (i.e., peculiar velocities) can have a non-negligible effect on the projected distance calculations for the smaller redshift values. Therefore, we account for this prior to the search of close companions by applying the flow model of Tonry et al. (2001) to derive the redshifts corrected for peculiar velocities and linearly tapering to the observed values between $z = 0.02$ and 0.03 . A similar approach can be found in Baldry et al. (2012). Unless stated differently, from now we will be always using and referring to the corrected redshifts. Next, to select close pairs (i.e., stage 1 of the merger sequence) we made our main query in the NSA catalog and complemented it with SDSS DR18. We looked for the closest companion within a projected radius of $r_p = 50$ kpc and velocity separation lower than $|\Delta v| \leq 300$ km s⁻¹ with respect to the MaNGA galaxies. The projected radius was calculated considering the peculiar velocity corrected redshifts, while for the velocity separation we used the observed (non-corrected) redshifts. In this step, we are only considering galaxies that have not been already classified as any merger stage. Since we are focusing on the effects of interaction on our main sample, which is composed of MaNGA galaxies, the mass ratio is computed as $\mu = M_{\star M}/M_{\star c}$, where $M_{\star M}$ and $M_{\star c}$ are the stellar masses of the MaNGA and the companion galaxies, respectively. In order to avoid extremely minor interactions, we restricted the search to companions that yielded a mass ratio $\mu \leq 10$ based on their NSA Petrosian stellar mass (in the case of SDSS we applied this restriction after deriving the stellar mass, as explained in Sect. 2.3). We also used the mass ratio to classify as major mergers those with $\mu \leq 4$, while those with $\mu > 4$ were classified as minor mergers (e.g. Lotz et al. 2011; Ellison et al. 2013). When applicable, we also discarded those cases where $\chi_r^2 > 5$ for either the MaNGA galaxy or the companion, where χ_r^2 is the goodness of fit reduced χ^2 value resulting from the spectral energy distribution (SED) fitting (see Sect. 2.3). In order to further increase the classification quality, the projected separation, velocity separation, mass ratio and χ^2 restrictions were also applied to stage 2 galaxies. However since the tidal interaction can have an important effect on the measured mass ratio and luminosities, those with $\mu > 10$ or $\chi^2 > 5$ were not reclassified as stage 0, but instead they were simply excluded from the analysis. In addition, since we are interested in dwarf-dwarf interactions, we have excluded all galaxies with non-dwarf companions (i.e., companions with $M_{\star} \geq 10^{10} M_{\odot}$) from the galaxy interaction analysis (Sects. 3.1 and 3.2). Some of the companions in stages 1 and 2

were not found in NSA nor SDSS, but were identified via visual inspection and confirmed as being interacting with spectroscopic redshifts from the NASA Extragalactic Database (NED⁶) or, in those cases where the companion lies within the MaNGA IFU, from the spectra of the spaxels corresponding to the companion. We will be referring to these as the “manually found” galaxies. Finally, for a few cases where the companion galaxy did not have an available measured spectroscopic redshift and was not within the MaNGA IFU but had unambiguous signs of interaction with the respective MaNGA galaxy, the spectroscopic redshifts of the latter were assigned to the companions.

2.3. Correcting mass ratios

The stellar masses we used throughout this work are those provided in the MaNGA survey, which in turn are extracted from the NSA catalog. In some cases, the algorithm used in the NSA catalog under-deblends close objects (which we identified in the visual inspection process), which results in a stellar mass value that is actually a combination of both objects. In addition, some of the identified companions are not present in the NSA catalog, and therefore do not have an available NSA stellar mass value. To account for both of these problems, we took a similar approach to Steffen et al. (2023). We derived the stellar masses of all the affected galaxy pairs fitting their ultraviolet (UV) to mid-infrared (MIR) SED with CIGALE (Boquien et al. 2019). In particular we use GALEX far-UV and near-UV (Martin et al. 2005), SDSS *ugriz* (York et al. 2000), WISE W1-4 (Wright et al. 2010) and 2MASS JHK_s (Skrutskie et al. 2006). The photometric data gathering and treatment is described in Appendix A. Then we compute the mass ratio μ of each affected galaxy pair as:

$$\mu = \frac{M_{\star M}^{\text{SED}}}{M_{\star c}^{\text{SED}}}, \quad (2)$$

where $M_{\star M}^{\text{SED}}$ and $M_{\star c}^{\text{SED}}$ are the stellar masses obtained from the SED fitting of the MaNGA and companion galaxies, respectively. We then combine the mass ratio with the NSA stellar masses $M_{\star \text{NSA}}$ to compute the individual stellar masses of the under-deblended close pairs:

$$M_{\star M} = M_{\star \text{NSA}} \frac{\mu}{1 + \mu}, \quad (3)$$

$$M_{\star c} = M_{\star \text{NSA}} \frac{1}{1 + \mu}, \quad (4)$$

and for the case of the companions with missing NSA stellar masses:

$$M_{\star c} = \frac{M_{\star \text{NSA}}}{\mu}, \quad (5)$$

while the MaNGA stellar masses remain as $M_{\star M} = M_{\star \text{NSA}}$.

2.4. The galactic environment

In order to further explore the impact of the environment on AGN triggering and disentangle it from the effects of close interactions/mergers, we need to characterize the environment. There are several approaches in the literature to this end (e.g. Cooper et al. 2005; Baldry et al. 2006; Geha et al. 2012; Pearson et al. 2016; Yang et al. 2007; Argudo-Fernández et al. 2015, etc.). To have a wider perspective and be able to check for consistency, we have selected three different environmental factors for a galaxy: being isolated, in a void, or part of a group or cluster.

⁶ <https://ned.ipac.caltech.edu/>

2.4.1. Isolated galaxies

The presence of a nearby massive galaxy has been used as proxy to study the impact of the environment and the star formation rate (SFR) of dwarf galaxies as *isolated* and *non-isolated* (e.g. Geha et al. 2012; Stierwalt et al. 2015; Kado-Fong et al. 2020). In particular, Geha et al. (2012) found that the fraction of quenched dwarf galaxies strongly increases with lower projected separations to a massive galaxy ($M_{\star} \geq 2.5 \times 10^{10} M_{\odot}$), and remains constant at separations higher than 1.5 Mpc. Following the parameters and results of their work, we define a dwarf isolated galaxy as not having any massive galaxies within $|\Delta v| \leq 1000 \text{ km s}^{-1}$ and 1.5 Mpc of projected radius. The search for nearby massive galaxies was first performed within the NSA catalog considering the Petrosian stellar mass and then in the SDSS database using the *CasJobs* tool⁷ considering the `logMass_noMassLoss` column from the `stellarMasStarformingPort` table for the stellar mass value. A few potential massive neighbors found in SDSS had no available stellar mass values. For these cases we estimated the stellar mass using the formula and parameters provided in Roediger & Courteau (2015) for $g-r$. Since there might be a few massive neighbors that lie outside the footprint of SDSS (and therefore of NSA) we also searched in the 2MASS Extended Source Catalog (XSC; Jarrett et al. 2000) for sources with absolute magnitudes $M_{K_s} \leq 22.86$, which corresponds to the massive galaxy threshold assuming $(M_{\star}/L)_{K_s} = 0.95 M_{\odot}/L_{\odot}$ and $M_{K_s \odot} = 3.32$ (Bell et al. 2003). The redshifts for the 2MASS sources were obtained by crossmatching with several spectroscopic surveys⁸: NED, the 100% complete Arecibo Legacy Fast ALFA Survey (ALFALFA; Haynes et al. 2018), the 2dF Galaxy Redshift Survey (2dFGRS; Colless et al. 2001, 2003), the 6dF Galaxy Redshift Survey (6dFGS; Jones et al. 2004, 2009) and the CfA Redshift Survey (ZCAT⁹; Huchra et al. 1995). The applied k-correction was obtained using the code provided by (Chilingarian & Zolotukhin 2011), and the extinction was derived using the color excess $E(B-V)$ values of (Schlafly & Finkbeiner 2011) provided by the IRSA *Galactic Dust Reddening and Extinction* service¹⁰ and using $R_{K_s} = 0.306$ (Yuan et al. 2013). Finally, we matched the results from the 2MASS XSC with the NSA and SDSS and removed those galaxies that had been previously rejected in the NSA and SDSS. This yields a total of 2329 (~71% of the sample) non-isolated galaxies.

2.4.2. Galaxies in voids

To classify our galaxies as being located within a void or not we crossmatched our galaxy sample with that of Pan et al. (2012), who constructed a catalog of galaxies in voids using the *VoidFinder* algorithm (Hoyle & Vogeley 2002). All the matches were marked as being in a void in our sample. Next, to distinguish those galaxies that are not in a void from those that have non valid data, we crossmatched the rest of the galaxies from our sample to the parent catalog of the void sample, which is the Korea Institute for Advanced Study Value-Added Galaxy Catalog (KIAS-VAGC). The positive matches were then marked as not being in a void, while the rest of the galaxies were marked as non-valid (and will hence be excluded from any analysis re-

garding voids). This results in a total of 1013 (~31%) galaxies in voids, 2157 (~66%) not in voids and 110 (~3%) non-valid.

2.4.3. Groups and clusters

Similarly to the voids, we find if each of our galaxies belongs to a group or a cluster by crossmatching our sample with the *Self-calibrated Galaxy Group Catalog* (hereafter the Group Catalog; Tinker 2021, 2022), which includes the group richness (i.e. the number of members in the group) for each galaxy, which we will denote as G . Next, we divided the results in three categories: *Field galaxies* ($G = 1$, meaning the galaxy is not part of a group), *Group galaxies* ($2 \leq G \leq 50$) and *Cluster galaxies* ($G > 50$). We chose 50 as it is a typical value for the transition from groups to clusters (Abell 1958). This resulted in 1937 (~59%) field galaxies, 652 (~20%) group galaxies and 369 (~11%) cluster galaxies. The 322 (~10%) galaxies that had no match in the Group Catalog were excluded from any analysis regarding group richness.

2.5. Sources of incompleteness and biases

Given the parent surveys and magnitude ranges used in this work, there are several sources of incompleteness that can potentially affect the quality of our results, especially when considering the method for classifying galaxies in stage 1 (close pairs). Here we discuss how we have addressed each of them.

2.5.1. Magnitude limits and overall spectroscopic completeness

The majority of the companion galaxies we found come from either NSA and/or SDSS, the latter being the main (but not only) source of redshift values of the former. Consequently, there is a very significant drop in spectroscopic completeness (computed as $f_s = N_z/N_p$, where N_z and N_p are the number of spectroscopic and photometric¹¹ galaxies, respectively.) for r-band magnitudes $r \geq 17.77$, which is the magnitude limit for the SDSS spectroscopic sample (Strauss et al. 2002). This is illustrated in Fig. 5, which shows the spectroscopic completeness vs. the magnitude for both SDSS and NSA within a 300'' radius¹² of each galaxy of our sample. This magnitude limit results in an under-representation of galaxies with lower brightness (a.k.a. the Malmquist bias), and consequently of companions with lower masses and pairs of higher mass ratios (i.e. minor mergers), especially at higher redshifts. Table 1 shows estimations of the number of non-detected close companions due to flux limits for $\mu \leq 4$, $4 < \mu \leq 10$ and the total. The derivation of these values is mainly based on the magnitude difference and mass ratios of galaxy pairs, and is detailed in Appendix D. In principle, this under-representation could be compensated for by applying weights (analogous to the approach explained in Sect. 2.5.3). However, only a small portion (~8%, 22 galaxies in total) of the detected companions have magnitudes $r > 17.77$. Compensating weights based on such a small subset could lead to a more inaccurate representation of the underlying population. Moreover, we expect that this bias has little to no effect in our results, considering the following argument: If the magnitude limit affects both the AGNs and non-AGNs of our sample equally, we should

⁷ <https://skyserver.sdss.org/casjobs/>

⁸ Along with SDSS, these surveys are the sources for the redshifts in NSA.

⁹ <https://www.cfa.harvard.edu/~dfabricant/huchra/zcat/>

¹⁰ <https://irsa.ipac.caltech.edu/applications/DUST/>

¹¹ Since the photometry of NSA is based on SDSS, the number of photometric objects is the same for both surveys.

¹² We selected this radius since it provides sufficient sources to have a reliable measure of completeness while being very specific for our sample.

miss companions of AGN and non-AGN galaxies proportionally to the AGN fraction of the full sample. In other words, the AGN fraction in observed pairs should be equal to the AGN fraction in true pairs. This argument remains valid whether there is a correlation between close pairs and being an AGN or not. However, under the assumption that there is, in fact, such a correlation, the AGN fraction of observed single galaxies could differ from that of true single galaxies. This is because when counting as single galaxies those that are observed as single, but are in fact pairs, the included AGNs and non-AGNs are not proportional to the AGN fraction of the full sample. This situation is illustrated in Fig. 6, which shows a simulation of the AGN fraction distribution for true and observed galaxy pairs and non-pairs assuming $p_{TP} = 0.15$, $p_{obs} = 0.6$, and $p_{P-AGN} = 0.7$, where p_{TP} is the probability of having a true pair, p_{obs} is the probability of observing a pair and p_{P-AGN} is the probability that a paired galaxy is an AGN (assuming a positive correlation). Based on these probabilities we generate a sample of 1000 galaxies to measure the AGN fraction, and then repeat this process 500 times to obtain the AGN fraction distribution. Notice that the p-value p_{z-test} obtained from the z-test performed to compare the means of the true and observed distributions is well above the commonly accepted significance level $\alpha = 0.05$, suggesting the true and observed pairs distributions have the same mean, although the observed distribution has a higher uncertainty. The behavior remains qualitatively the same for different values of p_{TP} , p_{obs} and p_{P-AGN} (even when allowing them to vary for each iteration), with the only relevant difference being the separation for the observed and true singles and the dispersion of observed pairs. In fact, the values used for this plot were chosen to accentuate this difference, since the values we have estimated yield an even smaller (but still statistically significant) difference. Fortunately, not only does this difference tend to be small, but also, since it is present only in the AGN fraction of single galaxies, it is averaged out when combining with the other control galaxies (see Sect. 2.6). We also need to consider how this affects the early mergers/pairs fraction when comparing the AGN and non-AGN samples. Since the decrease in the early mergers/pairs fraction due to flux limits is proportional to the number of true early mergers/pairs, the stronger the AGN-merger correlation is, the more prominent is the effect of the non-detected pairs. This means that any difference found between the early mergers/pairs fractions of the AGN and non-AGN samples will be slightly attenuated. Nevertheless, based on our estimations of the total of non-detected companions (see Table 1), we expect this effect to be small.

Lastly, we have to consider the overall completeness. We have measured a mean spectroscopic completeness of ~ 0.67 at $r \leq 17.77$ for both SDSS and NSA separately, and ~ 0.8 for their combination. This means that even below the magnitude limit, there is a 20% chance that we miss a close companion and consequently underestimate the distance to the closest companion or classify a close pair (i.e. stage 1) as a single galaxy (i.e. stage 0). Although this value is not negligible, it still represents a minority. More importantly, based on the argument above, it should not systematically affect our results for the AGN fraction.

2.5.2. The low-mass end

A consequence of the selection method for the MaNGA targets is that it is also affected by incompleteness in the low-mass end. According to Wake et al. (2017), the sample is virtually complete for stellar masses $M_{\star}^{p+} > 1.2 \times 10^9 M_{\odot}$ and $M_{\star}^s > 3.7 \times 10^9 M_{\odot}$ ¹³

¹³ These values have already been adjusted to our cosmology.

Table 1. Estimated numbers of non-detected close companions at mass ratio ranges corresponding to major ($\mu \leq 4$) and minor ($4 < \mu \leq 10$) mergers and the total. The number inside the brackets is the proportion corresponding to the total of the row.

Mass ratio range	Observed	Non-detected
$\mu \leq 4$	218 (0.95)	12 (0.05)
$4 < \mu \leq 10$	36 (0.65)	19 (0.35)
Total ($\mu \leq 10$)	254 (0.89)	31 (0.11)

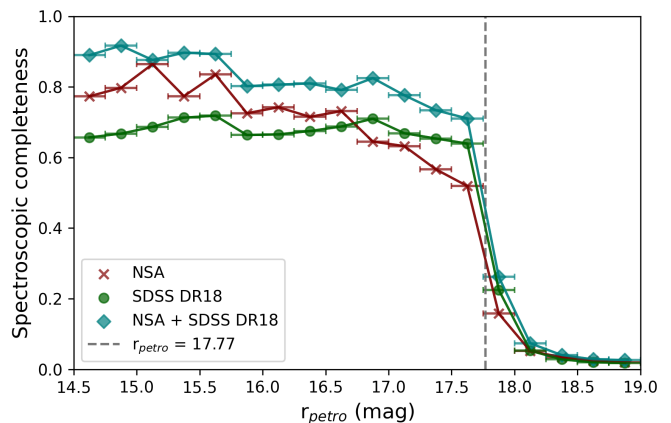


Fig. 5. Spectroscopic completeness vs r-band Petrosian magnitude in SDSS DR18 (green dots) and NSA (red crosses) and their combination (blue diamonds). The vertical line at $r_{petro} = 17.77$ shows the magnitude selection limit for the SDSS spectroscopic sample. The spectroscopic completeness was computed as the number of galaxies with spectra in SDSS or NSA respectively, over the number of galaxies with photometry in SDSS DR18 within a $300''$ radius of each galaxy of our sample.

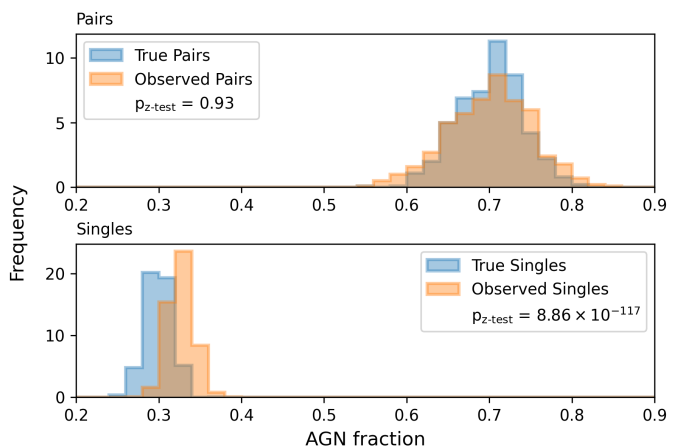


Fig. 6. The simulated AGN fraction distribution of true and observed galaxy pairs and single galaxies assuming the probabilities stated in the text for a sample size of 1000 galaxies and over 500 iterations. p_{z-test} indicates the p-value obtained from a two sample z-test performed on the true and observed distributions to test if they have the same mean value.

for the MaNGA *Primary+* and *Secondary* samples, respectively. Consequently, we remove all galaxies with stellar masses below these limits from the main sample. This affects 24 galaxies.

2.5.3. Fiber collisions (SDSS/NSA)

Another type of incompleteness that has a direct impact on galaxy close pairs comes from fiber collisions within the SDSS multi-object spectrograph, which permits a minimum angular separation of $55''$ (Blanton et al. 2003), meaning that the spectra of galaxy pairs with separations lower than this cannot be acquired simultaneously using a single spectroscopic plate. This minimum separation corresponds to 50 kpc at a redshift of $z \approx 0.048$, hence most of our sample is affected by it. There are regions, however, in which two or more plates overlap, meaning that a fraction of galaxy pairs with separations below $55''$ are recovered. To account for the remaining incompleteness we took an empirical approach similar to that of Patton & Atfield (2008), but adapted to our situation. First we made a spectroscopic sample by searching for all galaxies with spectra within a radius of $300''$ of each galaxy of our sample in both SDSS DR18 and NSA, combining the results of both samples and removing all redundant objects. We then made a photometric sample, by searching for all galaxies with photometry in SDSS DR18 within the same region. Since NSA is restricted to $z \leq 0.15$, in order to maintain consistency we removed all objects with $z > 0.15$ from both the spectroscopic and photometric samples (for the photometric sample we first matched it to the spectroscopic sample to know which objects were beyond the redshift limit). We then removed from both samples all the galaxies that are in our MaNGA sample, and added the manually found spectroscopic neighbors in order to prevent overcorrection. Next we computed the spectroscopic completeness (as explained in Sect. 2.5.1) at different angular separations, as shown in the top panel of Fig. 7. As expected, completeness decreases below $\theta = 55''$. To compensate for this, we multiply each pair below $\theta < 55''$ by a weight $w_\theta = f_s/g(\theta)$, where $g(\theta)$ is a function representing the best fitting line below $\theta = 55''$. In turn, all galaxy pairs with $\theta > 55''$ have been given a weight of $w_\theta = 1$. Notice that the bin width used in Fig. 7 is of $10''$. This was done to reduce the uncertainties and improve the fitting quality. Consequently, the fitting includes some galaxies that are between $55''$ and $60''$. Upon several tests, we found that was the best trade-off, as the fitting parameters show negligible differences. The bottom panel of Fig. 7 shows the effect of applying the correcting weights.

2.5.4. Close pair spaxel overcount

Another potential bias that we detected comes from the AGN selection method used in Mezcuca & Domínguez Sánchez (2024). Since they only selected sources with more than 20 AGN spaxels in their final classification, close pairs in which the companion is partially or completely within the MaNGA field are more likely to be included, since the companion spaxels would be counted as well. Upon visually checking all potentially affected galaxies, we found only one case (9490-12701; shown in Fig. E.1) where the main galaxy has less than 20 AGN spaxels, however we did not exclude it from the sample since this galaxy is particularly small with respect to its MaNGA field (possibly due to an IFU allocation based on an under-deblended close pair), meaning that the proportion of AGN spaxels is relatively high.

2.6. Control sample

In order to isolate the effect of close pairs/mergers on AGN fraction and further account for possible remaining biases, we have constructed a control sample matched in stellar mass and redshift. For this purpose, we separated our sample into two subsets:

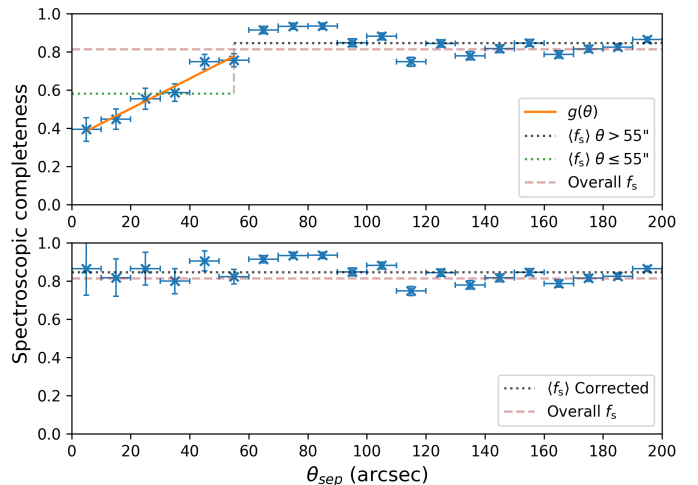


Fig. 7. Spectroscopic completeness vs. angular separation for the SDSS DR18 and NSA combined. *Top:* The data before applying the weight correction. The spectroscopic completeness noticeably decreases from $\theta = 55''$ to smaller separations, while for $\theta > 55''$ it converges towards the overall spectroscopic completeness ($f_s \approx 0.83$). The solid orange line shows the fit to the data below $\theta = 55''$. In order to improve the fitting quality and reduce error sizes we have used $10''$ wide bins. Consequently, we are also including a few galaxies between $55''$ and $60''$ for the fitting. *Bottom:* The data after applying the weight correction. The spectroscopic completeness was computed in the same way as in Fig. 5. The error bars were computed by error propagation.

the interacting galaxy sample, composed of galaxies in stages 1-5, and the control pool, composed of galaxies at stage 0. To account for potential environmental effects, we add a restriction so that galaxies can only be matched to those with the same condition of being isolated and being in a void¹⁴, then find the best simultaneous match in stellar mass and redshift to each galaxy of the interacting sample from the control pool and run a Kolmogorov–Smirnov (KS) test between the interacting sample and the matched controls. Following the criterion of Ellison et al. (2011), if the KS probability is above 0.3, we keep that control sample and repeat the process to find the next best match. This process is repeated until either the KS probability reaches a value of 0.3 or lower, or we reach 10 iterations. In our case the second condition was met first. Note that although an interacting galaxy can only be matched to a certain control galaxy once, the control galaxies can be matched to several interacting galaxies.

3. Results and discussion

3.1. AGN fraction throughout the merger process

We first compare the AGN fraction of paired/merger galaxies to the respective control group at different bins of projected separation between pairs, as shown in the top panel of Fig. 8. The AGN fraction of galaxy pairs at projected separations below 20 kpc (where pairs with tidal features become the dominant population) starts to increase notoriously, reaching a value of 0.85 (1.42 times the AGN fraction of the control group in the respective bin) below 10 kpc. Then, the AGN fraction peaks with 0.89 at stage 3 (merger) and remains high throughout the rest of the merger process, although slightly decreasing towards the final

¹⁴ Here we have omitted the field, group or cluster criterion because the matching became too restricted, resulting in some galaxies with zero matches.

stage. This behavior is consistent with that observed for massive galaxy dominated samples (e.g. Ellison et al. 2011; Satyapal et al. 2014; Barrows et al. 2023), but paired massive galaxies start to show AGN excess at higher separations. This indicates that the AGN-merger connection does extend to the low-mass domain, but the triggering separation scales down with stellar mass. Interestingly, when comparing the AGN fraction of all merger stages (bottom panel of Fig. 8) we find a distinct AGN fraction boost for stages 2-5. To confirm this we grouped stages 0-1 and 2-5 and performed a χ^2 -test of independence with which we found a very significant statistical difference between both groups ($p_{\chi^2} = 6 \times 10^{-9}$)¹⁵. Although this is consistent with the top panel of Fig. 8, as we expect to find more galaxies in stage 2 than stage 1 at smaller separations (and vice-versa for larger separations), it also suggests that only interactions from the first pass onwards trigger AGNs.

We further investigated the effect of potential contamination by star formation emission in the AGN selection, and repeated the entire process removing the SF-AGN galaxies from our sample (Fig. C.1). After removing the SF-AGN, the AGN fractions are lower in general but a similar trend remains, having a higher AGN population for close pairs/mergers. In this case the same χ^2 -test yielded a smaller but still significant difference ($p_{\chi^2} = 0.04$), although the AGN fraction boost seems to already take place at stage 1 (i.e. before the first pass). This is possibly due to the fact that galaxies at stage 1 have the lowest SFR values in the merger sequence (see Fig. C.4), meaning that the AGN fraction at this stage is likely less affected by the removal of SF-AGN from the sample. This could also explain the notorious drop for stage 4. Although the literature about AGNs in dwarf galaxy mergers is very scarce, we found that our results are in agreement with Mićić et al. (2024), who reported an enhancement in the frequency of X-ray identified AGN of grouped/paired dwarf galaxies when compared to non-interacting dwarf galaxies. Similarly, La Marca et al. (2024) found an AGN excess in mergers compared to non-mergers based on MIR, X-ray and SED AGN identification methods, and in all their redshift bins. Although their work is not restricted to dwarf galaxies, their stellar mass distribution vs. redshift plot seems to indicate that in their lowest redshift bin ($0.1 \leq z < 0.31$) the stellar masses of the dominant population are within $10^9 - 10^{10} M_{\odot}$. This AGN excess in mergers has also been observed at much higher redshifts ($5.3 \leq z < 6.7$) by Duan et al. (2024) based on BPT and SED selection methods, and with a sample mostly composed of galaxies with $M_{\star} < 10^{10} M_{\odot}$. Considering the variety of sources and AGN selection methods, the evidence supporting an AGN-merger connection in the dwarf galaxy regime is quite robust, and we find that possibly this connection becomes observable from the first pass of the merger.

3.2. The interacting fraction of AGNs

In the previous section we showed that dwarf-dwarf mergers can trigger AGNs, however this is not a complete view on the merger-AGN connection. We now combine our samples the other way around. Figure 9 shows the fractions of single galaxies (stage 0), pairs and early mergers (stages 1 and 2) and advanced mergers (stages 3-5) for the AGN and non-AGN samples, respectively. At first glance, it is fairly obvious that mergers are not the primary cause of AGN triggering, as they do not account

¹⁵ We also performed a post-hoc test which yielded seemingly consistent results, however some of the differences become much less significant due to the small size of some individual categories.

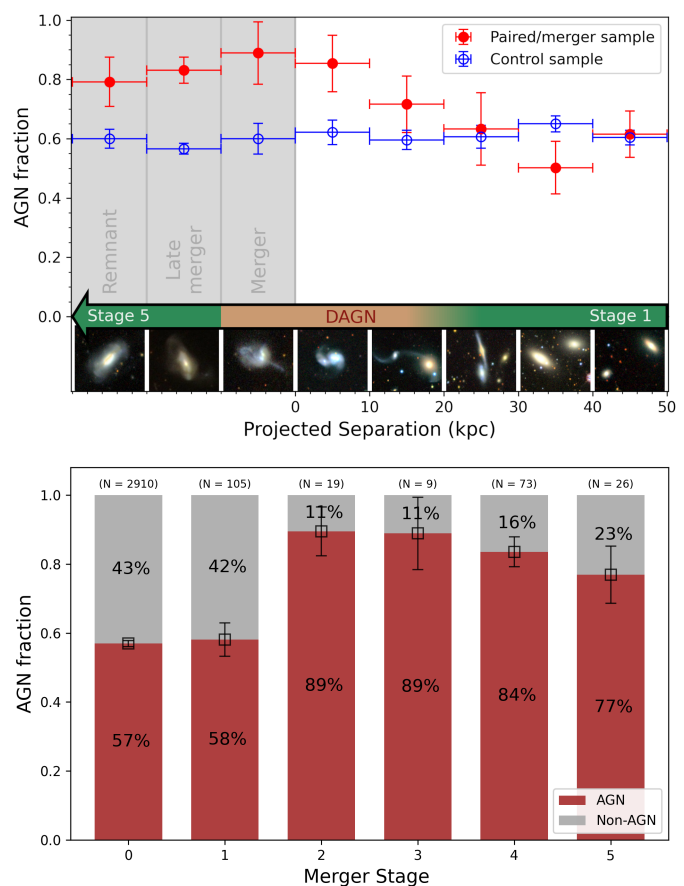


Fig. 8. *Top panel:* the AGN fraction vs. the projected separation for the paired/merger sample (filled red points) and its control group (open blue points). The horizontal bars show the bin width, while the vertical bars show the binomial error of each bin. The gray bins at the left of the 0 kpc mark correspond to stages 3, 4 and 5 from right to left, respectively. The green arrow shows the direction of evolution of the merger process, and the orange region inside of it indicates the range in which we could expect to find dual AGNs (note that the right end is a gradient, since the condition of being a dual AGN will depend on the applied definition and more factors than only the projected separation.). The galaxy images below the arrow are representative examples of the corresponding bin. Notice that stages 1 and 2 are mixed in the projected separation region. *Bottom panel:* the AGN fraction at each merger stage, shown as a percentage. The error bars show the binomial error of each bin. The numbers on top indicate how many AGNs are in the corresponding bin. Notice that the AGN fraction for stages 3-5 might slightly vary from the top plot because a few galaxies were excluded from the latter, since they did not have a valid value for the Void criterion, and hence could not be matched to control galaxies.

for 90% of the AGNs in our sample. Nevertheless, there seems to be a higher prevalence of advanced mergers in the AGN sample. This is confirmed by performing χ^2 -tests considering only advanced mergers, pairs and early mergers, and the combination; for which the results can be found in Table 2, including the effect size (calculated as the φ coefficient), which measures how strong is the correlation between the categorical variables. Considering a typical significance level of 0.05, the p-values obtained indicate that the difference in advanced mergers fraction is statistically significant, while for pairs and early mergers is not. In all cases we have φ values below 0.2, which indicates a weak effect size. We also derived the merger excess for each

Table 2. The p-values and effect size (measured by the φ coefficient) obtained from the χ^2 -tests, and merger excess for different merger groups.

Group	p_{χ^2}	φ	Merger excess
(Full Sample)			
Advanced mergers	3×10^{-7}	0.09	3.38 ± 0.85
Early mergers/pairs	0.361	0.02	1.20 ± 0.22
All mergers/pairs	1.6×10^{-5}	0.08	1.83 ± 0.26
(Without SF-AGN)			
Advanced mergers	0.061	0.04	1.91 ± 0.61
Early mergers/pairs	0.054	0.04	1.54 ± 0.33
All mergers/pairs	0.005	0.06	1.65 ± 0.29

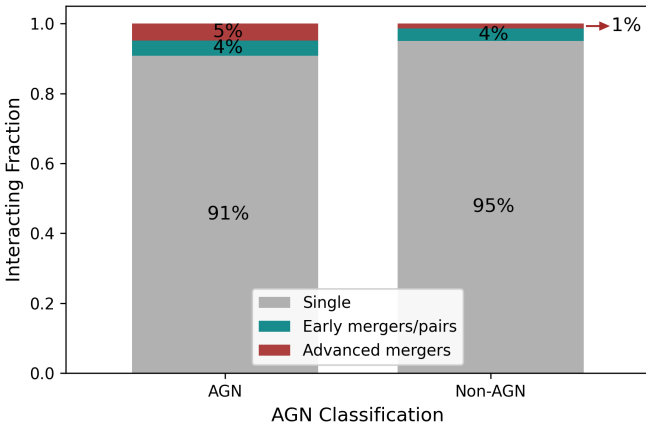


Fig. 9. The fraction of single (stage 0), early mergers/pairs (stages 1-2) and advanced mergers (stages 3-5) in the AGN and non-AGN samples.

case, computed as the merger fraction in AGNs divided by that in non-AGN controls. These excess values we obtained are highly consistent with those found by La Marca et al. (2024) and at higher redshift by Duan et al. (2024). On the other hand, Kaviraj et al. (2019) found no merger excess in their dwarf galaxy AGN sample when compared to a control non-AGN sample, by selecting AGNs based on WISE infrared photometry. Similar results are reported by Bichang’a et al. (2024), who identified AGNs via SED fitting. Although the origin of these discrepancies is not entirely clear, it should be noted that the sample sizes of Kaviraj et al. (2019) and Bichang’a et al. (2024) are considerably smaller ($N < 900$) than those of La Marca et al. (2024) ($N = 69140$ for the lowest redshift bin), Duan et al. (2024) ($N = 3330$), and this work. Additionally, considering the effect sizes we found, our results are not incompatible with those of Kaviraj et al. (2019) and Bichang’a et al. (2024).

It is worth noting that the interaction fractions of the respective AGN samples vary considerably among these works. This is possibly in part due to the differences in stellar mass distribution range, and most likely due to the different AGN identification techniques, since the amount of detected AGNs varies considerably depending on the selected method (e.g. see Calderón-Castillo & Smith 2024). More importantly, in the majority of cases, merger fractions in the AGN samples tend to be (well) below 0.5, indicating that most AGNs in dwarf galaxies are not triggered by merger events, meaning that secular processes are a more likely channel for AGN ignition.

3.3. The role of the environment

We now investigate the impact of the environmental factors on the presence of AGNs in dwarf galaxies. Figure. 10 shows the AGN fraction of our sample for galaxies that are isolated, in voids and part of a group/cluster. We find a consistent trend in all three factors: the AGN fraction tends to be higher for galaxies located in less dense environments. We confirm this by performing χ^2 -tests to determine the statistical differences in the AGN fractions of the samples of each factor, as shown in Table 3. Since the group richness factor has more than two categories, its effect size is measured by the Cramér V instead of the φ coefficient. Except for field vs. group galaxies, all differences are statistically significant, although with a weak effect size ($\varphi, V < 0.2$). These results indicate that being part of a cluster has the strongest effect on dwarf galaxy quenching. This is in agreement with Witherspoon & Wilcots (2024), who identified AGNs by applying the [NII]-BPT and [SII]-BPT diagrams on a sample also extracted from MaNGA (although using a stellar mass limit of $M_{\star} \leq 10^{9.7} M_{\odot}$) and found that low-mass galaxies hosting AGNs are more likely to be found in isolation or in low-mass groups in comparison to non-AGN galaxies. Simulations also agree with our results. For instance, using ILLUSTRISTNG, Kristensen et al. (2021) found a preference for higher density environments for non-AGN dwarf galaxies. Similar results were reported by Tremmel et al. (2024) using the ROMULUS cosmological simulation, who found that dwarf galaxies in clusters are less likely to host X-ray luminous AGNs than those in the field. In contrast, several observational works report no significant difference between the environments of AGN and non-AGN dwarf galaxies. For example, Kristensen et al. (2020) identified AGNs based on emission-line fluxes in a sample of 62258 dwarf galaxies and did not find any environmental difference between AGN and non-AGN dwarf galaxies in the local Universe. Similar results were reported by Manzano-King & Canalizo (2020), and also by other authors who identified AGNs based on radio emissions (Davis et al. 2022), SED fitting (Bichang’a et al. 2024) or even combinations of methods at different wavelengths (Siudek et al. 2022). Particularly for voids, Liu et al. (2015) report that AGNs in voids are similarly abundant to those in walls. We note that this is the only instance we could find in the literature that includes the stellar mass range of dwarf galaxies, however the mass distribution of their “faint sample” also includes a good portion of non-dwarf galaxies ($M_{\star} > 10^{10} M_{\odot}$), meaning that the present work is effectively the first to report the AGN fraction of dwarf galaxies in voids.

Interestingly, some authors have found that the AGN fraction actually increases in higher density environments using samples that include but are not limited to dwarf galaxies. For instance, Peluso et al. (2022) observed a significantly higher AGN incidence in galaxies undergoing ram pressure stripping, which happens most efficiently in clusters and massive groups (Hester 2006); and Hashiguchi et al. (2023) found that the AGN fraction of cluster galaxies is always higher than that of field galaxies, however in both cases it is possible that the results are mainly driven by the non-dwarf galaxy portion of the respective samples.

Similarly to the previous sections, we investigate if the discrepancies between our results and those mentioned above are related to SF contamination, by removing the SF-AGN from our sample. Unlike the case of mergers, we actually find a qualitative difference in the results, as shown in Fig. C.3: except for voids, the AGN fraction of dwarf galaxies is now higher for denser environments. A possible explanation for this is that the SFR

Table 3. The p-values and effect size (measured by the φ and Cramér V coefficients) obtained from the χ^2 -tests for each environmental factor. Field, Group and Cluster share the same value for V . The post hoc p-values were derived using the Benjamini-Hochberg correction.

Factor	P_{χ^2}	P_{χ^2} -post hoc	φ	V
Isolated/Non	1×10^{-6}	-	0.08	-
In Void/Non	2×10^{-7}	-	0.09	-
Field/Group	-	0.68	-	-
Field/Cluster	-	2×10^{-10}	-	0.12
Group/Cluster	-	2×10^{-7}	-	-

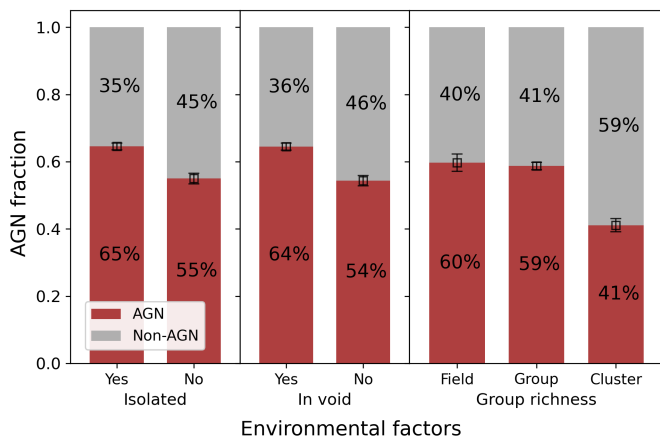


Fig. 10. The AGN fraction for the three environmental factors used in this work. In all three cases, the AGN fraction decreases with higher population density conditions

of dwarf galaxies tends to decrease in denser environments, as suggested by Fig. C.5 and observed by other authors (e.g. Geha et al. 2012; Stierwalt et al. 2015 although contradicting results were found by Siudek et al. 2022), since as a consequence SF-AGN galaxies are more likely to be concentrated in the lower density environments than composite and robust AGN galaxies. This drastic change could also explain the differences between the results shown in Fig. 10 and the aforementioned works since, except for Peluso et al. (2022) and Witherspoon & Wilcots (2024) (the results of the latter being consistent with ours), none of them use IFU spectroscopy, which has the advantage of being able to reveal the presence of AGNs that may be missed by other methods (Mezcua & Domínguez Sánchez 2020, 2024). The discrepancy between our work and Peluso et al. (2022) is possibly due to the fact that they only used the [NII]-BPT diagram to identify AGNs, which in our case would result in all SF-AGN being classified as just SF (see Sect. 2.1 and Mezcua & Domínguez Sánchez 2024).

4. Summary and conclusions

We have used a sample of 3280 dwarf galaxies from the MaNGA survey that were classified by Mezcua & Domínguez Sánchez (2024), as hosting (or not) an AGN based on three emission line diagnostic diagrams (the [NII]-, [SII]- and [OI]-BPT) and the WHAN diagram. We arranged the sample in a six-stage merger sequence arranged from earlier to later stages, based on visual inspection, projected separation ($r_p \leq 50$ kpc) and velocity difference ($|\Delta v| \leq 300$ km s $^{-1}$) to assess if dwarf-dwarf mergers trigger AGNs, by measuring the AGN fraction throughout the merger process and comparing it to a control group of non-merger and

non-paired galaxies matched in stellar mass, redshift, being isolated and in being in a void. We also study the contribution of mergers on AGN triggering by measuring the merger fraction in the AGN and non-AGN subsets. In addition, we investigate how the AGN fraction is affected by three environmental factors: isolation, voids and group richness. Our main findings are summarized as follows:

1. We observe an increase in the AGN fraction of paired/merger galaxies at separations below 20 kpc. This increase is higher at smaller separations, reaching an AGN fraction of 85% (1.42 times higher than the respective control group bin) at $r_p < 10$ kpc. The AGN fraction peaks at stages 2 (i.e. after the first pass) and 3 (i.e. two distinct nuclei within a common envelope) and remains enhanced until the latest merger stage (remnant). This shows that dwarf-dwarf interactions can ignite AGNs, independently of being isolated or in a void.
2. There is a significant boost on the AGN fraction of stage 2 mergers, suggesting that the triggering of AGNs occurs mainly from the first pass to posterior interactions.
3. Compared to its non-AGN counterpart, the AGN sample shows a merger excess of 3.38 for advanced mergers, 1.2 for early mergers/pairs and 1.83 for all mergers/pairs. The differences in the fractions of advanced mergers and all mergers/pairs between the AGN and non-AGN samples are statistically (very) significant, but with a weak effect size.
4. Even though dwarf galaxy mergers can trigger AGNs, the majority of AGNs are not ignited by merger events, leaving secular processes as the more likely AGN triggering mechanism.
5. The observed merger-AGN connection is very unlikely to be caused by SF contamination, as it remains qualitatively similar when removing all SF-AGN galaxies.
6. AGN activity in dwarf galaxies seems to be less prevalent in higher density environments, especially in galaxy clusters. This trend, although statistically significant, has a weak effect size for all three environmental factors.
7. Since the environment likely has an effect on the SFR, the method and criteria chosen for identifying and selecting AGNs can be critical to determine the relation between AGNs and the environment of dwarf galaxies.

Further complementary studies on the AGN fraction in dwarf galaxy mergers using a more extended survey such as DESI, which contains dwarf AGN candidates at 2.5-5 magnitudes fainter and at 10 times further in redshift than those detected in SDSS (Pucha et al. 2024), will provide more complete and statistically robust results. Furthermore, these studies can be expanded to investigate the AGN (and dual AGN) prevalence and activity in both the dwarf and massive galaxy regimes at different redshifts and considering different factors (e.g. environment, morphology, etc.). This will be crucial to have a more complete and precise model of the AGN-merger relation and the influence of the environment on AGN activity. In addition, the sample used in this work contains 17 dual AGN candidates (such as the one displayed in Fig. 2), for 12 of which a detailed analysis including awarded Chandra X-ray observations and VLBI radio observations will be presented in a fore-coming paper. The results from these works will provide key constraints on the mass of seed black holes, which is necessary to determine the SMBH formation scenario.

Acknowledgements. M.M. and A.E. acknowledge support from the Spanish Ministry of Science and Innovation through the project PID2021-124243NB-C22. M.S. acknowledges support by the State Research Agency of the Spanish Ministry of Science and Innovation under the grants

“Galaxy Evolution with Artificial Intelligence” (PGC2018-100852-A-I00) and “BASALT” (PID2021-126838NB-I00) and the Polish National Agency for Academic Exchange (Bekker grant BPN/BEK/2021/1/00298/DEC/1). HDS acknowledges financial support by the RyC2022-030469-I grant, funded by MCIN/AEI/10.13039/501100011033 and FSE+. VRM acknowledges support from the Spanish Ministry of Science, Innovation and Universities through the project PRE2022-104649. This work was partially supported by the program Unidad de Excelencia María de Maeztu CEX2020-001058-M and the European Union’s Horizon 2020 Research and Innovation program under the Maria Skłodowska-Curie grant agreement (No. 754510). This work used public data from the Sloan Digital Sky Survey (SDSS), NASA-Sloan Atlas (NSA), Two Micron All Sky Survey (2MASS), Wide-field Infrared Survey Explorer (WISE), Galaxy Evolution Explorer (GALEX) and the NASA/IPAC Extragalactic Database (NED; DOI: 10.26132/NED1) and Infrared Science Archive (IRSA; DOI: 10.26131/IRSA537). Funding for the SDSS IV has been provided by the Alfred P. Sloan Foundation, the Heising-Simons Foundation, the National Science Foundation, and the Participating Institutions. SDSS acknowledges support and resources from the Center for High-Performance Computing at the University of Utah. SDSS telescopes are located at Apache Point Observatory, funded by the Astrophysical Research Consortium and operated by New Mexico State University, and at Las Campanas Observatory, operated by the Carnegie Institution for Science. The SDSS web site is www.sdss.org. SDSS is managed by the Astrophysical Research Consortium for the Participating Institutions of the SDSS Collaboration, including Caltech, The Carnegie Institution for Science, Chilean National Time Allocation Committee (CNTAC) ratified researchers, The Flatiron Institute, the Gotham Participation Group, Harvard University, Heidelberg University, The Johns Hopkins University, L’Ecole polytechnique fédérale de Lausanne (EPFL), Leibniz-Institut für Astrophysik Potsdam (AIP), Max-Planck-Institut für Astronomie (MPIA Heidelberg), Max-Planck-Institut für Extraterrestrische Physik (MPE), Nanjing University, National Astronomical Observatories of China (NAOC), New Mexico State University, The Ohio State University, Pennsylvania State University, Smithsonian Astrophysical Observatory, Space Telescope Science Institute (STScI), the Stellar Astrophysics Participation Group, Universidad Nacional Autónoma de México, University of Arizona, University of Colorado Boulder, University of Illinois at Urbana-Champaign, University of Toronto, University of Utah, University of Virginia, Yale University, and Yunnan University. Funding for the NASA-Sloan Atlas has been provided by the NASA Astrophysics Data Analysis Program (08-ADP08-0072) and the NSF (AST-1211644). The Two Micron All Sky Survey is a joint project of the University of Massachusetts and the Infrared Processing and Analysis Center/California Institute of Technology, funded by the National Aeronautics and Space Administration and the National Science Foundation. WISE is a joint project of the University of California, Los Angeles, and the Jet Propulsion Laboratory/California Institute of Technology, and NEOWISE, which is a project of the Jet Propulsion Laboratory/California Institute of Technology. WISE and NEOWISE are funded by the National Aeronautics and Space Administration. The GALEX mission was developed by NASA in cooperation with the Centre National d’Etudes Spatiales de France and the Korean Ministry of Science and Technology. The NASA/IPAC Extragalactic Database and Infrared Science Archive are funded by the National Aeronautics and Space Administration and operated by the California Institute of Technology. We also acknowledge the use of images from the Legacy Surveys; full acknowledgments can be found here: <http://legacysurvey.org/acknowledgment/>. This work made use of Astropy (<http://www.astropy.org>): a community-developed core Python package and an ecosystem of tools and resources for astronomy (Astropy Collaboration et al. 2022).

References

Abdurro’uf, Accetta, K., Aerts, C., et al. 2022, *ApJS*, 259, 35
 Abell, G. O. 1958, *ApJS*, 3, 211
 Aihara, H., AlSayyad, Y., Ando, M., et al. 2019, *PASJ*, 71
 Amiri, A., Tavasoli, S., & De Zotti, G. 2019, *ApJ*, 874, 140
 Argudo-Fernández, M., Verley, S., Bergond, G., et al. 2015, *A&A*, 578, A110
 Astropy Collaboration, Price-Whelan, A. M., Lim, P. L., et al. 2022, *ApJ*, 935, 167
 Baldry, I. K., Balogh, M. L., Bower, R. G., et al. 2006, *MNRAS*, 373, 469–483
 Baldry, I. K., Driver, S. P., Loveday, J., et al. 2012, *MNRAS*, no
 Barrows, R. S., Comerford, J. M., Stern, D., & Assef, R. J. 2023, *ApJ*, 951, 92
 Belfiore, F., Maiolino, R., Maraston, C., et al. 2016, *MNRAS*, 461, 3111
 Bell, E. F., McIntosh, D. H., Katz, N., & Weinberg, M. D. 2003, *ApJS*, 149, 289–312
 Bianchi, L., Herald, J., Efremova, B., et al. 2011, *Ap&SS*, 335, 161–169
 Bianchi, L., Shiao, B., & Thilker, D. 2017, *ApJS*, 230, 24
 Bichang’a, B., Kaviraj, S., Lazar, I., et al. 2024, *MNRAS*, 532, 613–621
 Blanton, M. R., Bershady, M. A., Abolfathi, B., et al. 2017, *AJ*, 154, 28
 Blanton, M. R., Lin, H., Lupton, R. H., et al. 2003, *AJ*, 125, 2276–2286

Blecha, L., Snyder, G. F., Satyapal, S., & Ellison, S. L. 2018, *MNRAS*, 478, 3056–3071
 Bonnarel, F., Fernique, P., Bienaymé, O., et al. 2000, *A&AS*, 143, 33
 Boquien, M., Burgarella, D., Roehly, Y., et al. 2019, *A&A*, 622, A103
 Calderón-Castillo, P. & Smith, R. 2024, *A&A*, 691, A82
 Chilingarian, I. V. & Zolotukhin, I. Y. 2011, *MNRAS*, 419, 1727–1739
 Cid Fernandes, R., Stasińska, G., Schlickmann, M. S., et al. 2010, *MNRAS*, 403, 1036–1053
 Colless, M., Dalton, G., Maddox, S., et al. 2001, *MNRAS*, 328, 1039–1063
 Colless, M., Peterson, B. A., Jackson, C., et al. 2003, *ArXiv e-prints* [[arXiv:astro-ph/0306581](https://arxiv.org/abs/astro-ph/0306581)]
 Conselice, C. J., Bershady, M. A., Dickinson, M., & Papovich, C. 2003, *AJ*, 126, 1183–1207
 Conselice, C. J., Bershady, M. A., & Jangren, A. 2000, *ApJ*, 529, 886–910
 Conti, A., Bianchi, L., & Shiao, B. 2011, *Ap&SS*, 335, 329–331
 Cooper, M. C., Newman, J. A., Madgwick, D. S., et al. 2005, *ApJ*, 634, 833–848
 Davis, F., Kaviraj, S., Hardcastle, M. J., et al. 2022, *MNRAS*, 511, 4109–4122
 Deason, A., Wetzel, A., & Garrison-Kimmel, S. 2014, *ApJ*, 794, 115
 Dey, A., Schlegel, D. J., Lang, D., et al. 2019, *AJ*, 157, 168
 Domínguez Sánchez, H., Margalef, B., Bernardi, M., & Huertas-Company, M. 2021, *MNRAS*, 509, 4024–4036
 Driver, S. P., Bellstedt, S., Robotham, A. S. G., et al. 2022, *MNRAS*, 513, 439–467
 Duan, Q., Li, Q., Conselice, C. J., et al. 2024, *ArXiv e-prints* [[arXiv:2411.04944](https://arxiv.org/abs/2411.04944)]
 Ehlert, S., der Linden, A. v., Allen, S. W., et al. 2013, *MNRAS*, 437, 1942–1949
 Ellison, S. L., Mendel, J. T., Patton, D. R., & Scudder, J. M. 2013, *MNRAS*, 435, 3627–3638
 Ellison, S. L., Patton, D. R., Mendel, J. T., & Scudder, J. M. 2011, *MNRAS*, 418, 2043–2053
 Fakhouri, O., Ma, C.-P., & Boylan-Kolchin, M. 2010, *MNRAS*, 406, 2267–2278
 Geha, M., Blanton, M. R., Yan, R., & Tinker, J. L. 2012, *ApJ*, 757, 85
 Goulding, A. D., Pardo, K., Greene, J. E., et al. 2019, *ApJL*, 879, L21
 Gunn, J. E., Siegmund, W. A., Mannery, E. J., et al. 2006, *AJ*, 131, 2332–2359
 Hashiguchi, A., Toba, Y., Ota, N., et al. 2023, *PASJ*, 75, 1246–1261
 Haynes, M. P., Giovanelli, R., Kent, B. R., et al. 2018, *ApJ*, 861, 49
 Hester, J. A. 2006, *ApJ*, 647, 910–921
 Hopkins, P. F., Hernquist, L., Cox, T. J., et al. 2006, *ApJS*, 163, 1–49
 Hoyle, F. & Vogeley, M. S. 2002, *ApJ*, 566, 641–651
 Huchra, J. P., Geller, M. J., & Corwin, Harold G., J. 1995, *ApJS*, 99, 391
 Jarrett, T. H., Chester, T., Cutri, R., et al. 2000, *AJ*, 119, 2498–2531
 Jones, D. H., Read, M. A., Saunders, W., et al. 2009, *MNRAS*, 399, 683–698
 Jones, D. H., Saunders, W., Colless, M., et al. 2004, *MNRAS*, 355, 747–763
 Kado-Fong, E., Greene, J. E., Greco, J. P., et al. 2020, *AJ*, 159, 103
 Kauffmann, G., Heckman, T. M., Tremonti, C., et al. 2003, *MNRAS*, 346, 1055–1077
 Kauffmann, G., White, S. D. M., Heckman, T. M., et al. 2004, *MNRAS*, 353, 713–731
 Kaviraj, S., Martin, G., & Silk, J. 2019, *MNRAS*, 489, L12–L16
 Kewley, L. J., Dopita, M. A., Sutherland, R. S., Heisler, C. A., & Trevena, J. 2001, *ApJ*, 556, 121–140
 Kewley, L. J., Groves, B., Kauffmann, G., & Heckman, T. 2006, *MNRAS*, 372, 961–976
 Kristensen, M. T., Pimbblet, K., & Penny, S. 2020, *MNRAS*, 496, 2577–2590
 Kristensen, M. T., Pimbblet, K. A., Gibson, B. K., Penny, S. J., & Koudmani, S. 2021, *ApJ*, 922, 127
 La Marca, A., Margalef-Bentabol, B., Wang, L., et al. 2024, *A&A*, 690, A326
 Larson, K. L., Sanders, D. B., Barnes, J. E., et al. 2016, *ApJ*, 825, 128
 Law, D. R., Westfall, K. B., Bershady, M. A., et al. 2021, *AJ*, 161, 52
 Li, W., Nair, P., Irwin, J., et al. 2023, *ApJ*, 944, 168
 Liu, C.-X., Pan, D. C., Hao, L., et al. 2015, *ApJ*, 810, 165
 Lopes, P. A. A., Ribeiro, A. L. B., & Rembold, S. B. 2017, *MNRAS*, 472, 409–418
 Lotz, J. M., Jonsson, P., Cox, T. J., et al. 2011, *ApJ*, 742, 103
 Maiolino, R., Scholtz, J., Witstok, J., et al. 2024, *Nature*, 630, E2–E2
 Man, Z.-y., Peng, Y.-j., Kong, X., et al. 2019, *MNRAS*, 488, 89–98
 Manzano-King, C. M. & Canalizo, G. 2020, *MNRAS*, 498, 4562–4576
 Maraston, C., Pforr, J., Henriques, B. M., et al. 2013, *MNRAS*, 435, 2764–2792
 Martin, D. C., Fanson, J., Schiminovich, D., et al. 2005, *ApJ*, 619, L1–L6
 Martin, G., Kaviraj, S., Laigle, C., et al. 2019, *MNRAS*, 485, 796–818
 Martini, P., Mulchaey, J. S., & Kelson, D. D. 2007, *ApJ*, 664, 761–776
 Mezcua, M. 2019, *Nature Astronomy*, 3, 6–7
 Mezcua, M. & Domínguez Sánchez, H. 2020, *ApJL*, 898, L30
 Mezcua, M. & Domínguez Sánchez, H. 2024, *MNRAS*, 528, 5252–5268
 Micić, M., Irwin, J. A., Nair, P., et al. 2024, *ApJL*, 968, L21
 Osborne, C., Salim, S., Boquien, M., Dickinson, M., & Arnouts, S. 2023, *ApJS*, 268, 26
 Pan, D. C., Vogeley, M. S., Hoyle, F., Choi, Y.-Y., & Park, C. 2012, *MNRAS*, 421, 926–934
 Pan, H.-A., Lin, L., Hsieh, B.-C., et al. 2019, *ApJ*, 881, 119

- Patton, D. R. & Atfield, J. E. 2008, *ApJ*, 685, 235–246
- Paudel, S., Smith, R., Yoon, S. J., Calderón-Castillo, P., & Duc, P.-A. 2018, *ApJS*, 237, 36
- Pearson, S., Besla, G., Putman, M. E., et al. 2016, *MNRAS*, 459, 1827–1846
- Peluso, G., Vulcani, B., Poggianti, B. M., et al. 2022, *ApJ*, 927, 130
- Pimblett, K. A., Shabala, S. S., Haines, C. P., Fraser-McKelvie, A., & Floyd, D. J. E. 2012, *MNRAS*, 429, 1827–1839
- Pucha, R., Juneau, S., Dey, A., et al. 2024, *ArXiv e-prints* [arXiv:2411.00091]
- Rodríguez-Gomez, V., Snyder, G. F., Lotz, J. M., et al. 2018, *MNRAS*, 483, 4140–4159
- Roediger, J. C. & Courteau, S. 2015, *MNRAS*, 452, 3209–3225
- Sabater, J., Best, P. N., & Argudo-Fernández, M. 2013, *MNRAS*, 430, 638–651
- Satyapal, S., Ellison, S. L., McAlpine, W., et al. 2014, *MNRAS*, 441, 1297–1304
- Schlafly, E. F. & Finkbeiner, D. P. 2011, *ApJ*, 737, 103
- Secrest, N. J. & Satyapal, S. 2020, *ApJ*, 900, 56
- Silverman, J. D., Kovač, K., Knobel, C., et al. 2009, *ApJ*, 695, 171–182
- Singh, R., van de Ven, G., Jahnke, K., et al. 2013, *A&A*, 558, A43
- Siudek, M., Mezcua, M., & Krywult, J. 2022, *MNRAS*, 518, 724–741
- Skrutskie, M. F., Cutri, R. M., Stiening, R., et al. 2006, *AJ*, 131, 1163–1183
- Smith, B. J., Campbell, K., Struck, C., et al. 2018, *AJ*, 155, 81
- Steffen, J. L., Fu, H., Brownstein, J. R., et al. 2023, *ApJ*, 942, 107
- Stierwalt, S., Besla, G., Patton, D., et al. 2015, *ApJ*, 805, 2
- Strauss, M. A., Weinberg, D. H., Lupton, R. H., et al. 2002, *AJ*, 124, 1810–1824
- Tamfal, T., Capelo, P. R., Kazantzidis, S., et al. 2018, *ApJL*, 864, L19
- Tanaka, M., Ikeda, H., Murata, K., et al. 2021, *PASJ*, 73, 735–746
- Tinker, J. L. 2021, *ApJ*, 923, 154
- Tinker, J. L. 2022, *AJ*, 163, 126
- Tony, J. L., Dressler, A., Blakeslee, J. P., et al. 2001, *ApJ*, 546, 681–693
- Toomre, A. 1977, in *Evolution of Galaxies and Stellar Populations*, ed. B. M. Tinsley & R. B. G. Larson, D. Campbell, 401
- Tremmel, M., Ricarte, A., Natarajan, P., et al. 2024, *OJAp*, 7
- Van Wassenhove, S., Volonteri, M., Walker, M. G., & Gair, J. R. 2010, *MNRAS*, 408, 1139–1146
- Volonteri, M. 2010, *A&AR*, 18, 279–315
- Vázquez-Mata, J. A., Hernández-Toledo, H. M., Avila-Reese, V., et al. 2022, *MNRAS*, 512, 2222–2244
- Wake, D. A., Bundy, K., Diamond-Stanic, A. M., et al. 2017, *AJ*, 154, 86
- Wild, V., Kauffmann, G., Heckman, T., et al. 2007, *MNRAS*, 381, 543–572
- Witherspoon, C. A. & Wilcots, E. M. 2024, *ApJ*, 961, 192
- Wright, E. L., Eisenhardt, P. R. M., Mainzer, A. K., et al. 2010, *AJ*, 140, 1868–1881
- Yan, R., Tremonti, C., Bershady, M. A., et al. 2015, *AJ*, 151, 8
- Yang, X., Mo, H. J., van den Bosch, F. C., et al. 2007, *ApJ*, 671, 153–170
- York, D. G., Adelman, J., Anderson, Jr., J. E., et al. 2000, *AJ*, 120, 1579–1587
- Yuan, H. B., Liu, X. W., & Xiang, M. S. 2013, *MNRAS*, 430, 2188–2199
- Zhang, R. & Yuan, H. 2022, *ApJS*, 264, 14

Appendix A: Photometric data for the SED fitting

In order to ensure the SED fitting quality for the galaxies that were not properly deblended or have no available stellar mass in the NSA catalog (see Sect. 2.3), we require as complete and reliable photometric data as available for our main sample and companion galaxies. The data collecting procedure for the different photometric bands used is detailed below.

Appendix A.1: SDSS

We used the SDSS *CasJobs* tool to find all photometric objects within $5''$ around each of the affected galaxies. Since in many cases the SDSS DR18 deblending algorithm interprets regions of a galaxy as a separate galaxy (generally with a very dim magnitude) we had to visually inspect all the detected photometric objects to make sure we select the correct one. In a very few cases where there was no adequate object or the photometry was flagged as unreliable, photometric values were inspected and taken from DR7. To have an optimal balance between the accuracies of color and total luminosity, we followed the same procedure of Maraston et al. (2013) and used the *model* magnitudes but scaled to the i-band *cmodel* magnitudes (or Petrosian magnitudes for the DR7 cases).

Appendix A.2: GALEX

Since many sources of our sample appear in different GALEX-based catalogs, we crossmatched with each one and combined the results by complementing the missing values (or replacing them when the following catalog had more complete values for the galaxy) in the following order: *Improved GALEX photometry of $z < 0.3$ SDSS galaxies* (Osborne et al. 2023), *Revised catalog of GALEX UV sources* (Bianchi et al. 2017), *Catalogs of unique GALEX sources from GALEX fifth data release (GR5;* Bianchi et al. 2011), and the GALEX public archive at MAST (Conti et al. 2011). The crossmatch radius used was $8''$, and all matches with a separation greater than $5''$ were visually inspected to ensure they were correctly matched.

Appendix A.3: allWISE/2MASS

The allWISE photometry was obtained by a simple crossmatch. In the case of 2MASS, we first used the XSC and then complemented it with the Point Source Catalog. The crossmatch radius and procedure for both surveys were the same as for GALEX.

Appendix A.4: Extinction

Finally, to correct for extinction we took the color excess values $E(B - V)$ of Schlafly & Finkbeiner (2011) from the NASA/IPAC IRSA *Galactic Dust Reddening and Extinction* service. We used the extinction coefficients R_{λ} from (Zhang & Yuan 2022) for all bands.

Appendix B: Finer stage classification

To achieve a more objective classification between stages 1-2 and 4-5 we make use of the morphological asymmetry parameter A (Conselice et al. 2000) as follows:

Appendix B.1: Stages 1 and 2

After the visual classification and pair selection procedures are performed, we review all galaxy pairs classified as stages 1 and 2. Those pairs that show unambiguous tidal features (especially bridges and tails) are directly classified as stage 2. In contrast, galaxy pairs that are clearly separated and show no signs of interaction are classified as stage 1. The remaining cases, which are not as unambiguous, are classified using an asymmetry threshold of $A = 0.35$ above which pairs are classified as stage 2, while those below it are classified as stage 1. This threshold was obtained empirically by choosing the value that gave the results that best matched the initial classification. We note that, although this value is the same that was used in Conselice et al. (2003) to distinguish mergers, this is likely coincidental since currently we are only considering early mergers. The asymmetry values for most of our sample were taken from the *MaNGA Visual Morphologies from SDSS and DESI images* value added catalog (Vázquez-Mata et al. 2022), however in those cases where the parameter $CAS_flag = 0$ or where there was a reasonable suspicion that the A value is erroneous (e.g. image contamination or values that were extreme or inconsistent with the image) we re-derived A from DESI r-band images using the python code *STATMORPH* (Rodríguez-Gómez et al. 2018) and performing the masking manually.

Appendix B.2: Stages 4 and 5

The procedure was similar to that of stages 1 and 2 except for the distinction by tidal features, since they can be present in both stages. The value obtained for the asymmetry threshold was $A = 0.21$. All galaxies with values higher than these were labeled as stage 4, while those with lower values were labeled as stage 5. Re-derivation of A was performed with the same criteria and as described for stages 1 and 2.

Figure B.1 shows a sample of 5 galaxies at each merger stage after the final classification.

Appendix C: The effects of removing SF-AGN

Here we show how our results are affected by removing the galaxies classified as SF-AGN from our sample, as discussed in Sect. 3. Figure C.1 shows the AGN fraction vs. the projected separation (top panel) and the AGN fraction at each merger stage (bottom panel), Fig. C.2 shows the merger fraction in the AGN and non-AGN subsets, and Fig. C.3 shows the AGN fraction for the three environmental factors used in this work. We also show the specific star formation rate (sSFR) distribution of each merger stage for the entire sample in Fig. C.4. As mentioned in Sect. 3.1 the lowest sSFR value corresponds to stage 1. Interestingly, this slight decrease of SFR at pre-first pass stages also appears in the works of Calderón-Castillo & Smith (2024) and Pan et al. (2019), and for mass ranges including dwarf galaxies, although similarly to this work, in both cases there is not a statistically significant difference.

Appendix D: Estimation of missing close companions due to flux limits

As stated in Sect. 2.2.2, all suitable companion galaxies for our sample should have mass ratios $\mu \leq 10$. This should also roughly correspond to a maximum magnitude difference, where

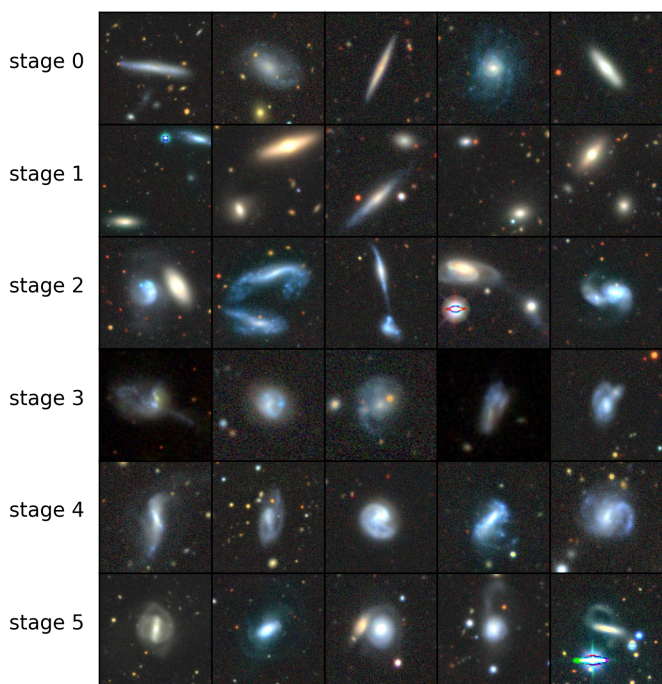


Fig. B.1. Examples of galaxy mergers at each stage after the final classification. All images are extracted from the DESI Legacy Survey, except for the first and fourth examples of stage 3, which were extracted from SDSS as this makes it easier to distinguish the nuclei for these two cases.

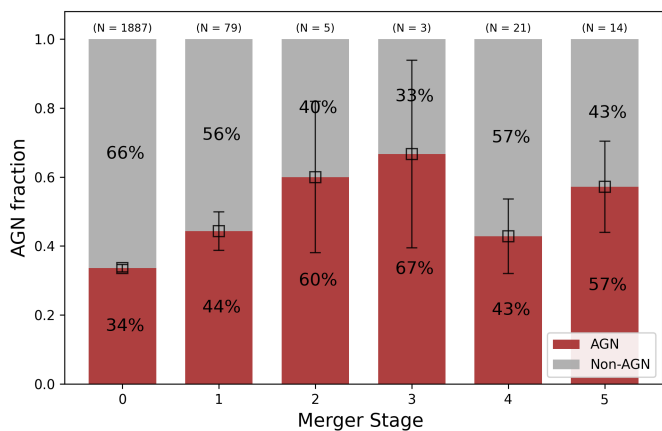
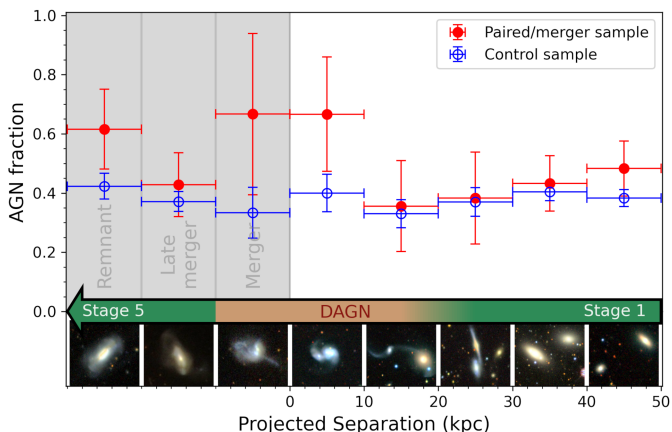


Fig. C.1. Same as Fig. 8 but after removing all galaxies classified as SF-AGN from our sample.

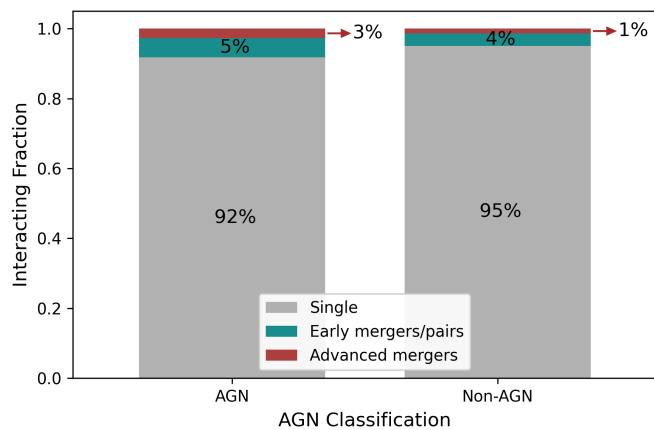


Fig. C.2. Same as Fig. 9 but after removing all galaxies classified as SF-AGN from our sample.

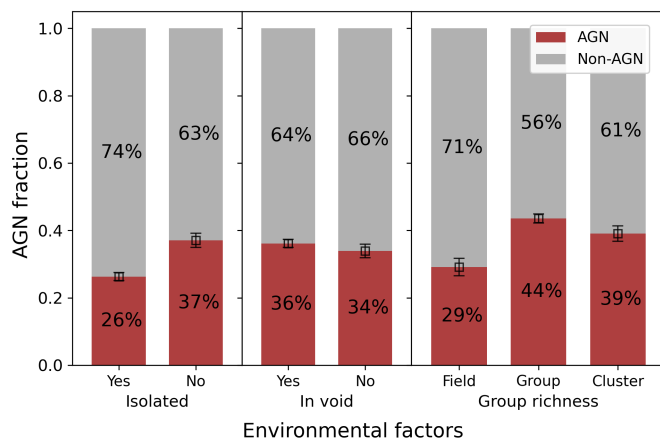


Fig. C.3. Same as Fig. 10 but after removing all galaxies classified as SF-AGN from our sample.

the brighter magnitude corresponds to the MaNGA galaxy of the pair. Based on this idea, we used all the close companions we found for our sample (including massive and secondary companions, which were excluded for the main analysis) to derive

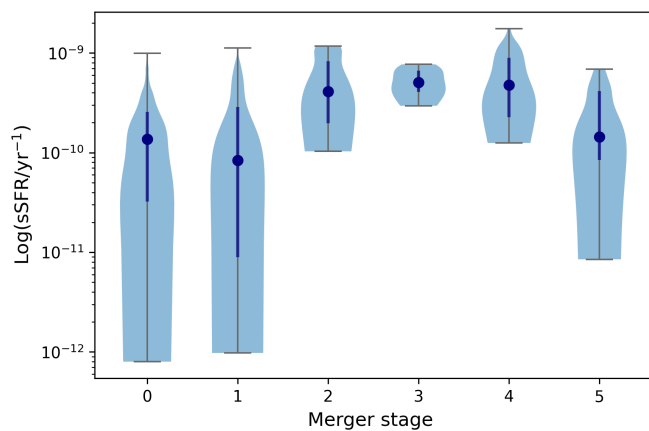


Fig. C.4. Violin plots of the specific star formation rate throughout the merger sequence. The blue circles indicate the median value, the thick blue line is the interquartile range and the thin gray bars show the distribution limits.

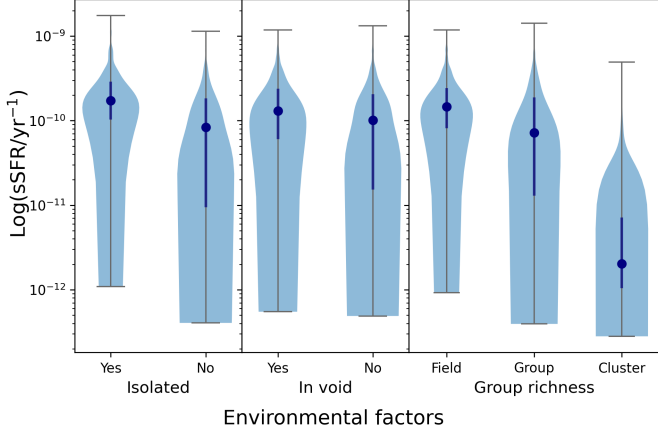


Fig. C.5. Violin plots of the specific star formation rate for the different environmental factors. The description is the same as in Fig. C.4.

an empirical correlation between the logarithm of the mass ratio and the difference in the r-band Petrosian magnitude:

$$\Delta r = (2.1 \pm 0.05) * \log(\mu) + (0.17 \pm 0.04). \quad (\text{D.1})$$

This equation corresponds to the best fitting line based on the Least Squares Method, which yielded a determination coefficient of $R^2 = 0.86$ and is displayed in Fig. D.1. From this relation we find that for $\mu = 10$, the maximum allowed magnitude difference is $\Delta r = 2.27$. We then apply this value to the r-band Petrosian magnitude of each galaxy in our MaNGA sample that is not a merger and has no detected companions (i.e. stage 0) to find how many could have a suitable companion that is beyond the detection limit ($r > 17.77$). We will refer to this group as the limit-affected subset and denote the number of members in it as N_A . Next, we define another subset made of those MaNGA galaxies that have a maximum allowed magnitude difference $\Delta r_{\text{max}} \leq 17.77$ (i.e. galaxies not affected by the flux limit) to derive the probability of having a suitable companion for our sample p_c as: (number of detected suitable companions of the subset)/(total number of galaxies in the subset). An important aspect to consider is that most galaxies are only affected partially by the flux limit, depending on their magnitude. For example, the search for a companion of a galaxy with a magnitude of $r = 16.0$ would only be affected by the flux limit for potential companions that yield a mass ratio greater than $\mu = 4.6$, which corresponds to the difference between the example galaxy and the SDSS limit according to Eq. D.1. This means that the potentially missing pairs correspond only to the portion of potential companions with a mass ratio greater than the corresponding limit. To find this portion, we modeled the mass ratio distribution of all observed suitable pairs as a gamma distribution as shown in Fig. D.2, for which the parameters were determined using the maximum likelihood estimation method. To assess the quality of the model we ran a KS-test between the model and the data, and obtained a p-value of ~ 0.6 , suggesting an adequate distribution model. The area under the distribution curve within $0 < \mu \leq 10$ is then normalized, so that given a certain mass ratio limit, we can calculate the portion affected by the flux limit (i.e. the area under the curve beyond the maximum observable mass ratio). We compute this portion for every galaxy of the limit-affected subset and obtain the mean value, which we denote as $p_{\mu\text{-lim}}$. Next, we have to consider that, although comparatively very few, there are galaxies detected at $r > 17.77$, which we should subtract from the final estimation. In order to do this, we use the ratio

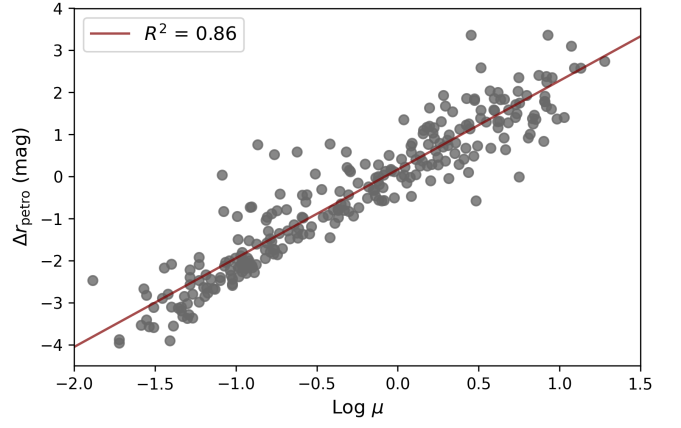


Fig. D.1. Relation between the Petrosian r-band magnitude differences of galaxies from the MaNGA dwarf sample and their companions and the logarithm of their respective mass ratio. The red line is the best fitting line to the data, corresponding to Eq. D.1.

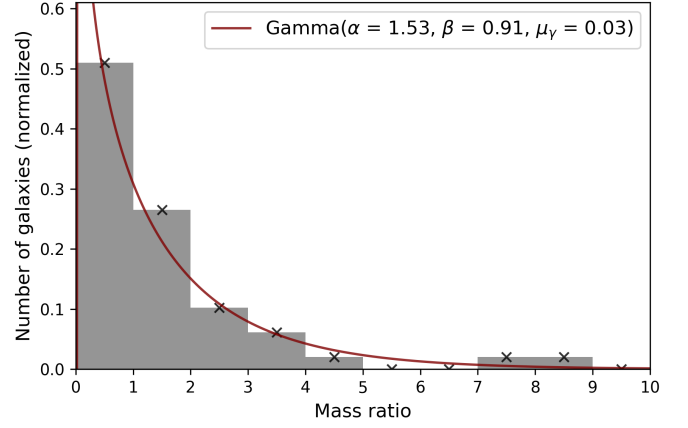


Fig. D.2. The mass ratio distribution of the galaxy pairs that are unaffected by the flux limit. The y axis is normalized so that the sum of all bins is 1. The black crosses show the center of the bin and the red line is the modeled gamma distribution with $\alpha = 1.53$, $\beta = 0.91$ and $\mu_\gamma = 0.03$, where α , β and μ_γ are the shape, scale and location parameters, respectively.

of the mean completeness values above and below $r = 17.77$ as $p_s = \int_s^{(17.77 < r \leq 20)} / \int_s^{(r \leq 17.77)}$, where we have taken $r = 20$ as the limit since it becomes extremely unlikely that one of our galaxies has a suitable companion at this magnitude. Finally, we estimate the total number of missing suitable companions as:

$$N_m = N_A * p_c * p_{\mu\text{-lim}} * (1 - p_s). \quad (\text{D.2})$$

We also did this entire procedure considering a maximum of $\mu = 4$ to be able to distinguish the ranges equivalent to those of major and minor mergers. The corresponding results can be found in Table 1.

Appendix E: Complementary images

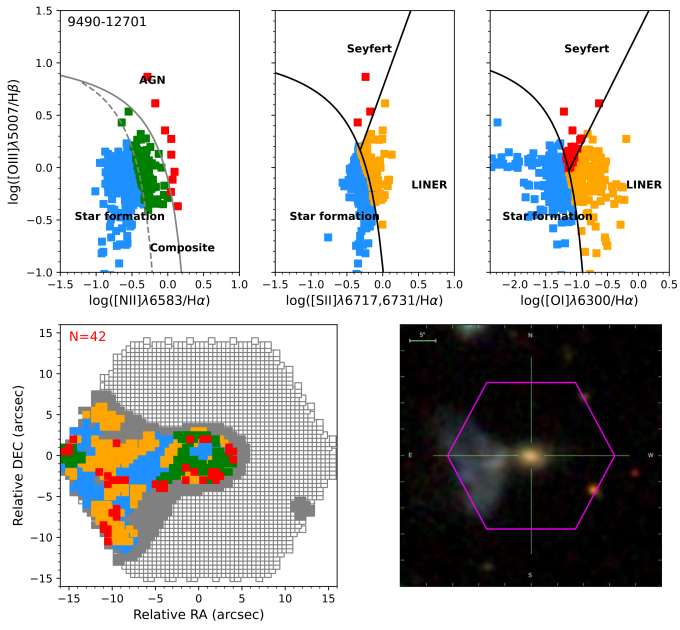


Fig. E.1. MaNGA analysis of the AGN dwarf galaxy 9490-12701. The description is the same as in Fig. 2. The main galaxy (located in the center of the MaNGA field) has less than 20 AGN spaxels, but the corresponding proportion of AGN spaxels is relatively high when considering the small portion of the MaNGA field that the galaxy occupies.